International Journal of Minerals, Metallurgy and Materials
Volume 24, Number 7, July 2017, Page 776
DOI: 10.1007/s12613-017-1461-y

Isothermal oxidation behavior and mechanism of a nickel-based superalloy at 1000°C

Zhi-yuan Zhu[1)], *Yuan-fei Cai*[1)], *You-jun Gong*[2)], *Guo-ping Shen*[2)], *Yu-guo Tu*[2)], *and Guo-fu Zhang*[2)]

1) School of Material Science and Engineering, Jiangsu University of Science and Technology, Zhenjiang 212003, China
2) Technology Center, Jiangsu Shenyuan Special Steel Co., Ltd., Xinghua 225722, China
(Received: 22 November 2016; revised: 11 February 2017; accepted: 15 Februery 2017)

Abstract: The oxidation behavior of a nickel-based superalloy at 1000°C in air was investigated through X-ray diffraction, scanning electron microscopy, and energy-dispersive spectroscopy analysis. A series of oxides, including external oxide scales (Cr_2O_3, (TiO_2 + $MnCr_2O_4$)) and internal oxides (Al_2O_3,TiN), were formed on the surface or sub-surface of the substrate at 1000°C in experimental still air. The oxidation resistance of the alloy was dependent on the stability of the surface oxide layer. The continuity and density of the protective Cr_2O_3 scale were affected by minor alloying elements such as Ti and Mn. The outermost oxide scale was composed of TiO_2 rutile and $MnCr_2O_4$ spinel, and the growth of TiO_2 particles was controlled by the outer diffusion of Ti ions through the pre-existing oxide layer. Severe internal oxidation occurred beneath the external oxide scale, consuming Al and Ti of the strength phase γ′ (Ni_3(Al,Ti)) and thereby severely deteriorating the surface mechanical properties. The depth of the internal oxidation region was approximately 35 μm after exposure to experimental air at 1000°C for 80 h.

Keywords: nickel-based superalloy; isothermal oxidation; oxide scale; internal oxidation

1. Introduction

Nickel-based superalloys are used as corrosion-resistant engineering materials for components intended for use in aggressive environments, such as gas turbine hot-section components, hot work tools, forging hammers, swaging dies, shear blades, and bolts and nuts. These superalloys exhibit excellent performance because of the satisfactory properties of Ni, which can be alloyed with other elements, such as Cr, Co, Mo, Fe, and W, over considerable concentration ranges without forming unstable, unsuitable, or detrimental phases [1–5].

Nickel-based superalloys containing 20wt% Cr show oxidation resistance because of the formation of an oxide scale of Cr_2O_3 on the alloy surface. The addition of Al and Ti improves the mechanical properties of the alloy through the formation of γ′ (Ni_3(Al,Ti)), which results in excellent castability, high creep strength, and rupture strength; the γ′ (Ni_3(Al,Ti)) functions as the principal hardening precipitate and exhibits a cube-on-cube orientation relationship to the matrix [6–7]. Exposure of metals to high-temperature environments induces the formation of corrosion products, leading to the loss of load-bearing cross-section, reducing reliability and stability, and shortening service lifetime of engineering components.

Engineers have devoted efforts to increasing the reaction temperature of fossil fuels in the cylinder chamber of internal combustion engines to achieve high energy efficiency and low emission of CO_2; as such, the demand for valve steel resistant to oxidation has increased. Nickel-based superalloys are the optimal candidate for such applications. The oxide scale becomes complex, rather than a simple continuous Cr_2O_3-rich oxide layer, at specific temperatures. Elements in the alloy diffuse to the substrate/air interface and accumulate at different positions, i.e., the upper chromium layer or the bottom layer, breaking the continuity of the outer protective oxide layer [8–10]. Unsuitable oxide products deteriorate the oxidation resistance of the alloy; as

Corresponding author: Zhi-yuan Zhu E-mail: salanganezhu@163.com

such, oxidation processes and their underlying mechanisms must be elucidated.

This research aims to investigate the evolution of the oxide scale formed on the nickel-based superalloy used as valve steel and exposed in experimental still air at 1000°C. X-ray diffraction (XRD) and energy-dispersive X-ray spectroscopy (EDS) were used to reveal the distribution of elements along the cross-section of the oxide scale.

2. Experimental

The nickel-based superalloy used in this study was supplied by Jiangsu Shenyuan Special Steel Company (China). The alloy was melted in a middle induction furnace under a vacuum atmosphere and was optimized by electro-slag remelting. The nominal composition (wt%) of the alloy was as follows: Cr 21.42, Al 1.97, Ti 2.76, Fe 2.13, Si 0.35, Mn 0.61, and Ni balance.

The alloy is commercially available as a 9.5-mm-diameter bar. The flank of the bar was polished in a turning lathe using metallographic abrasive papers to achieve a smooth side surface. The bar was then cut into 20-mm-long cylindrical specimens using a wire-cutting machine. The two remaining surfaces were ground on wet SiC paper and polished using 3.5-μm diamond paste to remove the damage caused by machining and produce a surface finish with an R_a of approximately 0.4 μm. All edges and corners were chamfered to reduce stress concentrators and polished to the same surface finish. The final dimensions after polishing were measured using a micrometer, and the surface area was calculated. The specimens were cleaned in ethanol, dried, and weighed on a calibrated balance with 0.1-mg precision (Sartorius BSA224S).

Isothermal oxidation testing was performed in a chamber furnace with experimental still air at 1000°C for 80 h. Batches of specimens were placed in alumina boats and inserted into the furnace at specified temperatures. The specimens were withdrawn at regular time intervals, and their mass change was measured. The oxide scale on the surface of the exposed specimen was directly identified through XRD analysis (Bruker D8 ADVANCE) using Cu K_α radiation; the samples were scanned over the 2θ range from 10° to 100°. The morphology of the oxide and the corresponding X-ray mappings of the alloying elements were examined by scanning electron microscopy (SEM: JEOL JSM-6480) in conjunction with EDS. The cross-sectional morphologies of the specimens were examined by SEM using backscattered electrons (BSEs), and the distribution of the alloying elements in the oxide scales and the substrate was assessed by EDS.

3. Results and discussion

3.1. Microstructure of the alloy substrate

Fig. 1 shows the microstructure of the specimen under SEM in the model of secondary electron; the specimen was etched in 10wt% oxalic acid for 60 s at an anode polarization potential of 6 V at room temperature. The compositions at points P_1 and P_2 are listed in Table 1. The element contents in P_2 are consistent with those in the matrix and Ti and Al elements are slightly enriched in some particles (similar to P_1) along the grain boundary.

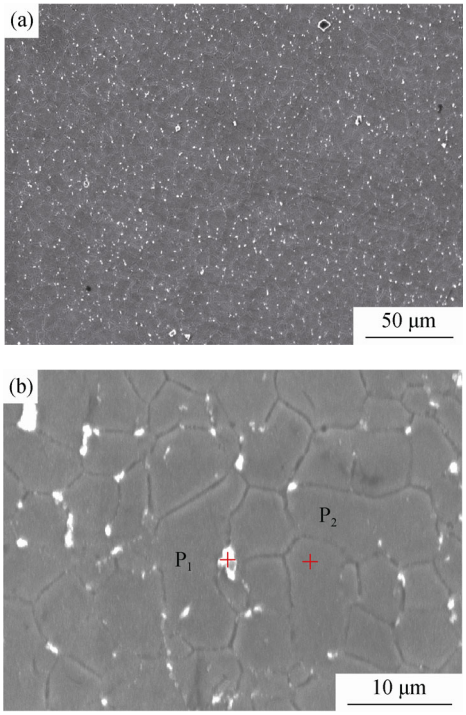

Fig. 1. SEM micrographs of the microstructure of the specimen after etching: (a) low magnification; (b) high magnification.

Table 1. Compositions at some topical points obtained by EDS analysis wt%

Position	Ni	Cr	Ti	Al	Si	Mn	Fe
P_1 in Fig. 2(b)	62.66	24.83	7.09	3.77	0.30	0.66	2.27
P_2 in Fig. 2(b)	71.19	21.42	2.68	1.68	0.19	0.52	2.32

No further heat treatment was applied to the specimens. The crystallite dimensions of the specimen are small, and a certain number of secondary phases are distributed along the

grain boundary; these phases will dissolve during the process of solution treatment and re-precipitate during the aging treatment with a different form. The types of precipitates and their generation processes are not the focus of the present research but will be investigated in our future work.

3.2. Weight-gain process

Fig. 2 shows the isothermal oxidation kinetics of the specimen at 1000°C as a plot of the specific mass gain versus exposure time. Under prolonged exposure, the curve becomes smoother after 48 h. The average oxidation rate during the 80-h period was 0.3981 $g \cdot m^{-2} \cdot h^{-1}$, which is not optimal. The curve can be described by

$$(\Delta m)^n = k_p t \quad (1)$$

where Δm is the specific mass gain ($mg \cdot cm^{-2}$), t is the exposure time (s), and k_p is the oxidation rate constant. We constructed a plot of the linear fit and obtained the best-fit value of n, which is 2.0721. The value is sufficiently close to 2; hence, parabolic kinetics can be assumed. Constant k_p is 4.0623×10^{-5} $mg^2 \cdot cm^{-4} \cdot s^{-1}$. These findings reveal that a continuous dense oxide scale can be generated on the specimen. The growth of the oxide scale is controlled by the diffusion of oxygen or alloying elements in the substrate after the formation of the continuous external oxide scale. At the initial stage of oxidation, the rate of weight gain is controlled by the reaction between the bulk elements and oxygen and is considered sufficient. In parallel, the consistency of the oxides is governed by oxygen potential. After the formation of a continuous and dense oxide layer, the diffusion of metal ions or oxygen becomes the rate-determining step of the oxidation reaction. The growth rates of Cr_2O_3 on pure Cr have been investigated in several studies, where the rate-determining step was found to be the outward diffusion of Cr ions through the Cr_2O_3 scale [3,5,8–9].

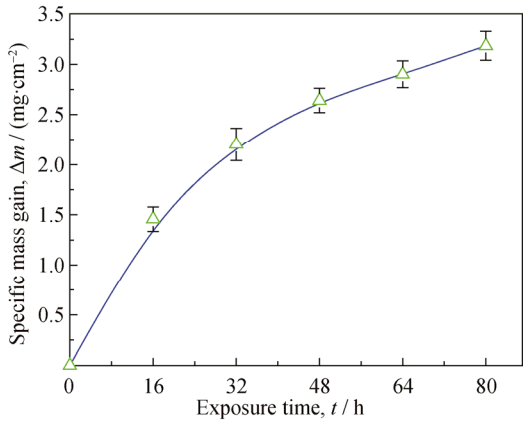

Fig. 2. Plot of specific mass gain of specimens against time at 1000°C.

3.3. Morphology of surface oxides

Fig. 3 shows the changes in the morphology of the surface oxides formed on the specimen under prolonged exposure at 1000°C. The surface oxides consist of two main types: columnar oxide particles and the underlying oxide scale. The scale breaks the continuity of the external oxide layer and contains defects, which serve as fast diffusion paths for oxygen. The columnar oxide particles gradually grow and become larger with increasing exposure time. The element compositions at some specific points are given in Table 2. Ti is generated in columnar particles, and the underlying oxide scale is composed of Cr and Mn. The phases of the oxide scale were confirmed by XRD analysis (Fig. 4). The surface oxides were identified as Cr_2O_3, TiO_2, and $MnCr_2O_4$ at each break time. At the initial stage of oxidation, these oxides formed at the substrate/air interface and can be detected during the entire exposure time. Moreover, the relative content of each oxide changes, the peak intensity of Cr_2O_3 decreases slightly, and the contents of TiO_2 rutile and $MnCr_2O_4$ spinel gradually increase with prolonged exposure time. These findings are consistent with those presented in Fig. 3. Hence, the columnar oxide particle is TiO_2 rutile, and the underlying oxide scale is mainly composed of $MnCr_2O_4$ spinel. Furthermore, the intensity of the substrate peaks decreases, indicating that the oxide scale becomes thicker and exceeds the penetration ability of the X-rays. Some sub-surface oxides could not be detected in the XRD scans because of their small volume fraction, although peaks associated with the substrate alloy were observed.

Columnar TiO_2 oxide particles were selected for calculation of their sizes using the Nano Measurer 1.2 software, as shown in Fig. 3(a); the grain size of more than 200 of these particles was measured at each time node. The histogram of particle size distribution and the curve of the average size versus exposure time are shown in Fig. 5. Under prolonged exposure time, the number of large TiO_2 particles increases, the average particle size of TiO_2 reaches 4.81 μm, and the maximum particle diameter exceeds 7 μm at 80 h. Consistent with the specific mass-gain curve (Fig. 2), the curve of increasing particle size (Fig. 5(a)) shows that the growth rate of the oxide particles decreases after 32 h. Thus, the growth of TiO_2 particles is mainly controlled by the outer diffusion of Ti ions through the pre-existing oxide layer. This result is in accordance with previous reports [8–9].

3.4. Oxide scale distribution and oxidation mechanism

The present nickel-based superalloy was severely oxidized at 1000°C. Oxides such as Cr_2O_3, TiO_2, and $MnCr_2O_4$

formed on the substrate. Fig. 6 shows the BSE images of the cross-section of the specimen oxidized at 1000°C for 80 h. The oxide layers show significant stratification along the cross-sectional direction and serious internal oxidation under the continuous external oxide layer. Fig. 7 shows the main element distribution in the cross-sectional profile of the specimen obtained by EDS map scanning. The results show that the main continuous and dense oxide layer contains a high concentration of Cr ions; the XRD analysis results confirmed the oxide layer to be Cr_2O_3.

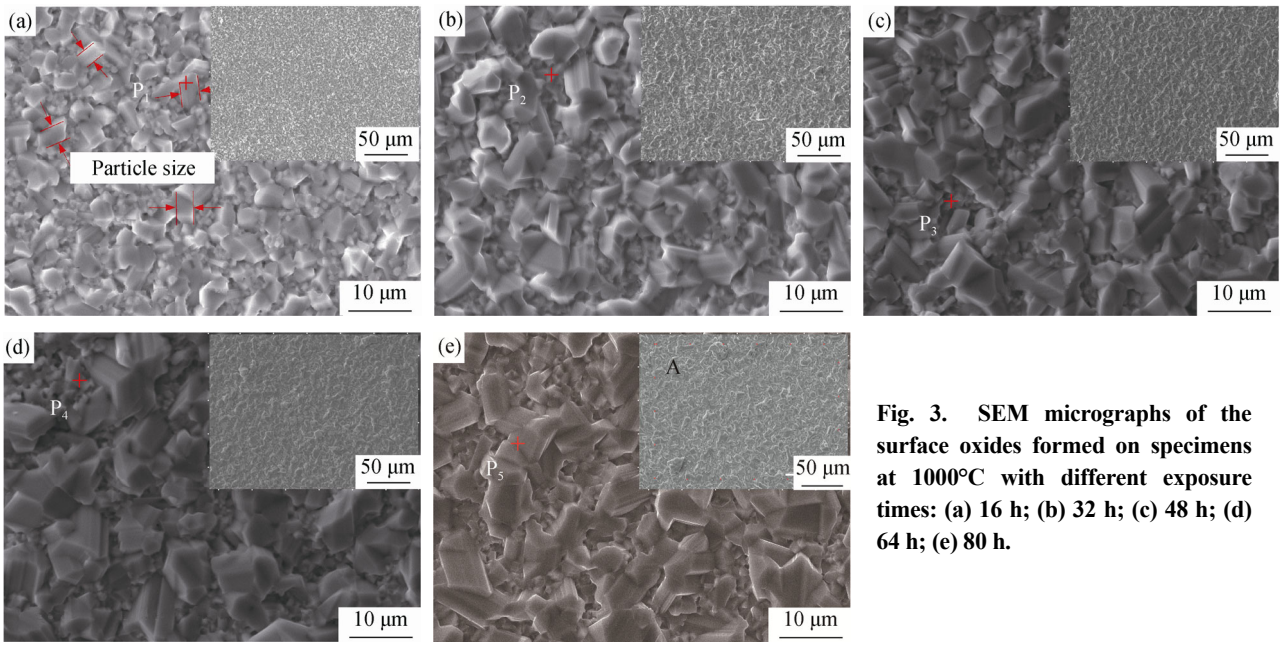

Fig. 3. SEM micrographs of the surface oxides formed on specimens at 1000°C with different exposure times: (a) 16 h; (b) 32 h; (c) 48 h; (d) 64 h; (e) 80 h.

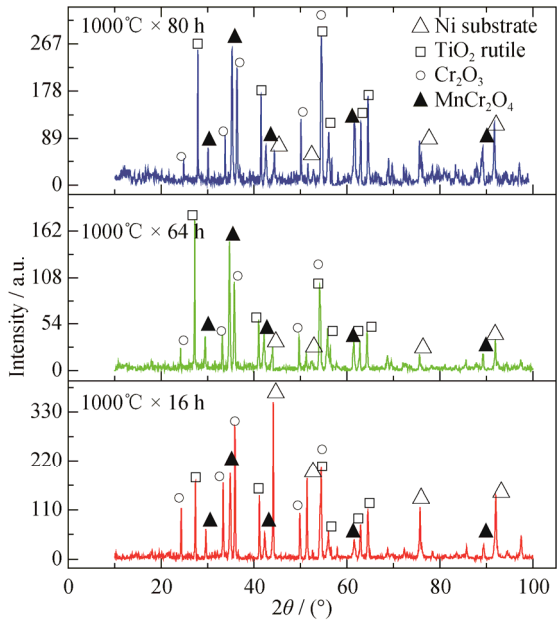

Fig. 4. XRD patterns of bulk thin oxide scales formed at 1000°C for 16 h (a), 64 h (b), and 80 h (c).

Furthermore, the internal dendritic oxide, which is distributed along the grain boundary, is concentrated with Al ions. Table 3 lists the elemental compositions of some topical points in the region detected by EDS. The Al ions are enriched in specific positions (similar to P_1 in Fig. 6(a)). A small number of Ti ions accumulated in the front of the Al-enriched region, and the content of oxygen ions did not increase, as illustrated by the red circles in Fig. 7. The authors of several studies [3,5,11–12] have reported that internal oxides are composed of Al_2O_3 and a small number of TiN, which consume the solvent atoms in the γ′ ($Ni_3(Al,Ti)$) phase in the sub-substrate; the region could be defined as the γ′ denuded zone. A deep γ′ denuded zone can substantially reduce the strength of the alloy surface and deteriorate the performance of engineering components. Fig. 8 shows the

Table 2. Compositions of some topical points obtained by EDS analysis wt%

Position	O	Ti	Cr	Mn
P_1 in Fig. 3	—	84.56	9.37	6.07
P_2 in Fig. 3	—	41.25	34.46	24.29
P_3 in Fig. 3	6.19	9.13	52.21	32.47
P_4 in Fig. 3	12.72	18.30	39.88	29.10
P_5 in Fig. 3	—	100.00	—	—
Region A in Fig. 3	11.80	47.91	21.57	18.72

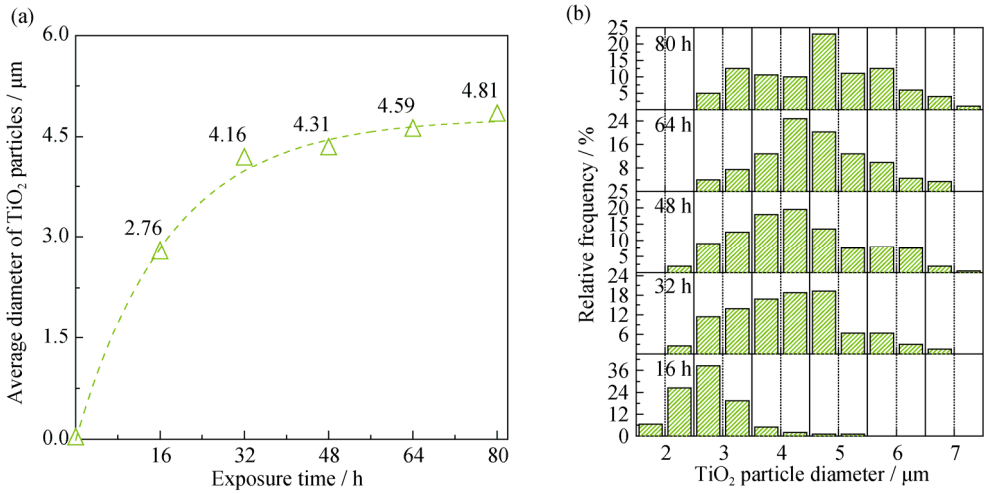

Fig. 5. Average diameter of TiO_2 particles at each time node (a) and distribution of TiO_2 particle sizes for different exposure times (b).

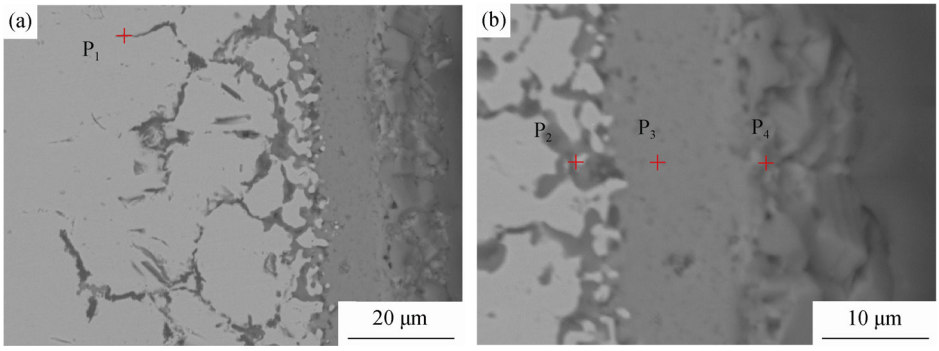

Fig. 6. Backscattered electron (BSE) images of the cross-section of a specimen oxidized at 1000°C.

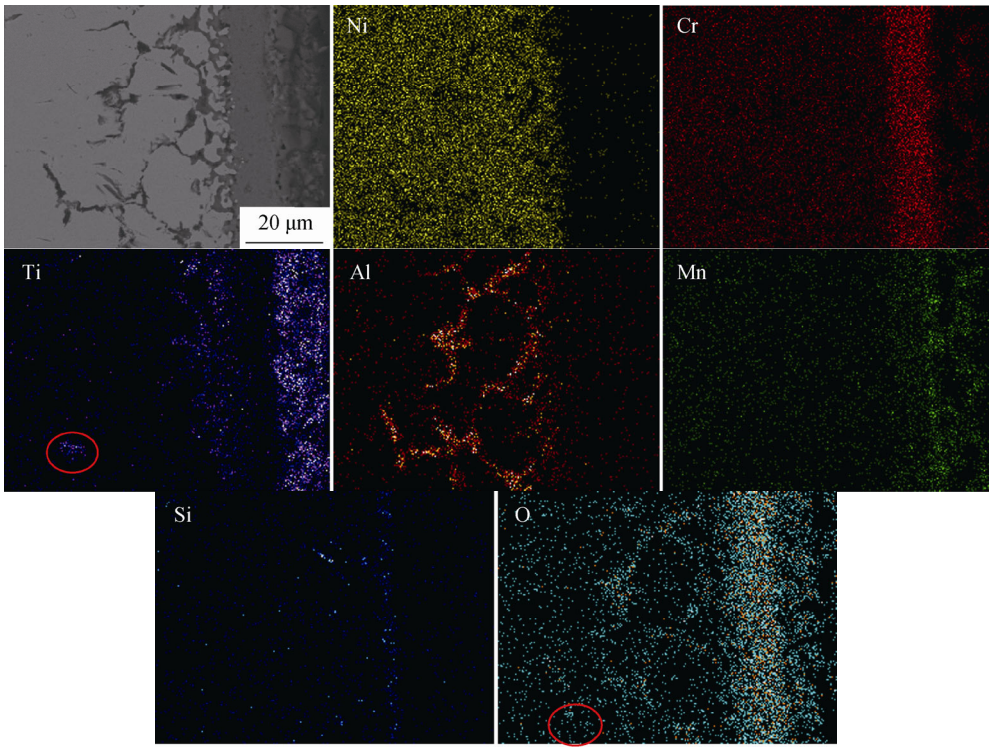

Fig. 7. BSE image and EDS maps of the section of a specimen maintained at 1000°C for 80 h; the EDS maps show the distribution of elements in the oxides formed, as indicated by the presence of oxygen.

standard Gibbs free energy profile of the oxidation reaction with 1 mol O_2 in the temperature range from 0 to 1200°C, as calculated using the HSC Chemistry 6.0 software; the specific values corresponding to 1000°C are listed in Table 4. The Al_2O_3 oxide exhibits the highest affinity for oxygen; however, it could only form along the internal grain boundary rather than a continuous external oxide layer. This limitation is a consequence of Al ions having a lower diffusion rate than Ti and Mn ions [13]; the stable oxide could easily form under extremely low oxygen potential, consuming the Al in the substrate. The grain boundaries serve as fast oxygen diffusion paths, and the internal oxidation of Al is controlled by the inward diffusion of oxygen ions through the external oxide layer and the grain boundary. The interface of the oxide/metal substrate is not plain, and an inward protuberance can be induced by several mechanisms, including interfacial tension, local differences in the drift velocity of the oxide lattice toward the alloy, and local differences in the thickness of the oxide layer [14–15].

Table 3. Compositions of some topical points obtained by EDS analysis wt%

Position	Ni	Cr	Ti	Al	Mn	Fe	O
P_1 in Fig. 6(a)	42.03	10.56	—	20.94	—	1.42	25.06
P_2 in Fig. 6(b)	17.73	33.41	4.43	3.05	—	—	40.06
P_3 in Fig. 6(b)	—	50.33	2.04	—	—	—	47.63
P_4 in Fig. 6(b)	3.02	21.87	7.24	—	22.42	—	45.45

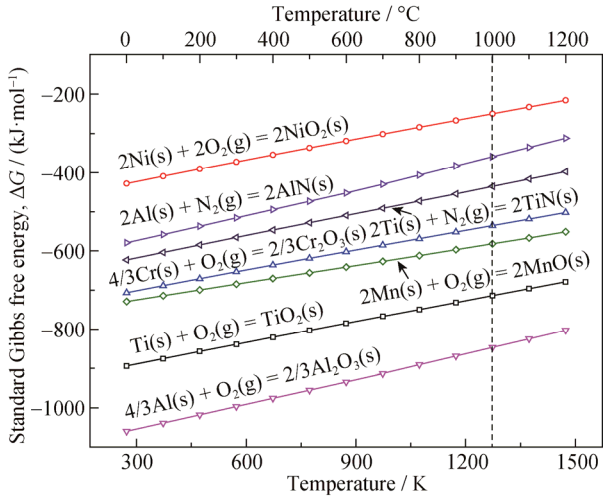

Fig. 8. Standard Gibbs free energy of the oxidation reaction with 1 mol O_2 or N_2 in the temperature range of 0–1200°C calculated using the HSC Chemistry 6.0 software.

The distribution of Ti is complex within the regions—specifically, the upper chromium layer, the bottom chromium layer, and the interior chromium layer. In these regions, Ti was consistently detected; the outermost region contains the highest concentration of Cr. Similarly, other authors [16–18] have noted that the Cr_2O_3 layer can dissolve a certain amount of Ti and form intermediate phases with complex compositions. The growth of the outermost TiO_2 particles is controlled by the outward diffusion of Ti ions through the pre-existing Cr_2O_3 oxide layer. Another study [11] confirmed that a certain number of $BCrO_3$ and $CrTi_2O_5$ phases were formed beneath the Cr_2O_3 layer, as determined by EBSD analysis of the cast nickel-based superalloy Rene 80. In our experiments, a B-rich region was not detected and the exact composition of the (Cr,Ti)-rich phase was not confirmed. According to Sigler's oxidation tests using Ti-modified Fe–20Cr alloys, a small amount of Ti (0.46wt%) increased the weight gain substantially [19]. In addition, Ti caused extensive internal oxidation within the sub-surface region of the chromia-forming alloy [3,12]. Therefore, the highly concentrated Ti might accelerate not only extensive internal oxidation but also the formation of a severely rugged oxide/metal substrate interface. In the present research, the outermost oxide layer is composed of TiO_2 and $MnCr_2O_4$ and is loose; it may speed up the inward diffusion of oxygen ions.

A small amount of Ni was detected in P_4 (Fig. 6(b)). This phenomenon may be occasional and can be attributed to the oxide of Ni. Research on the oxidation behavior of alloy 617 (0.04wt% Mn and 0.38wt% Ti) at 900°C revealed that the outer oxide layer is composed of Cr_2O_3, $NiCr_2O_4$, and NiO [5]. However, our calculations indicate that, as the Ti and Mn contents increase, the outermost oxide is replaced by $MnCr_2O_4$ and TiO_2 because the Gibbs free energy of NiO is higher than that of the other oxides (Table 4). In addition, we only detected Mn in the outermost oxide layer, and $MnCr_2O_4$ has been speculated to form from Cr_2O_3 and MnO with equal amounts of substance via solid-state reaction at 1000°C [20]:

$$Cr_2O_3\,(s) + MnO(s) = MnCr_2O_4(s) \quad (2)$$

Table 4. Standard Gibbs free energy of the oxidation reaction with 1 mol O_2 or N_2 at 1000°C calculated using the HSC Chemistry 6.0 software kJ·mol^{-1}

NiO	Cr_2O_3	TiO_2	Al_2O_3	MnO	TiN	AlN
–250.0	–535.4	–714.2	–847.0	–582.0	–435.3	–359.3

A continuous $MnCr_2O_4$ spinel layer that forms on the Cr_2O_3 scale can significantly increase the oxidation resistance of Haynes 230 (0.51wt% Mn and 0.01wt% Ti) at

900°C. Similarly, the authors of another study reported that the $MnCr_2O_4$ spinel layer improved the oxidation resistance of the bulk metal [21]. However, in the present study, the outermost oxide layer of the nickel-based superalloy (0.61wt% Mn and 2.76wt% Ti) is composed of TiO_2 and $MnCr_2O_4$, and the continuous layer is broken. A certain number of vacancies may exist in the oxide scale, and these vacancies can function as fast oxygen diffusion paths. Fig. 9 shows the EDS line-scanning map of the cross-sectional element distribution of the oxide layer at two break times: 16 and 80 h. The thickness of the outermost layer of the oxide may be enlarged during grinding as a consequence of the binding capacity of the resin. As oxidation progresses, the external oxide layer (Cr_2O_3, (TiO_2 + $MnCr_2O_4$)) does not substantially increase; by contrast, the internal oxide region increases from 8 to 35 μm.

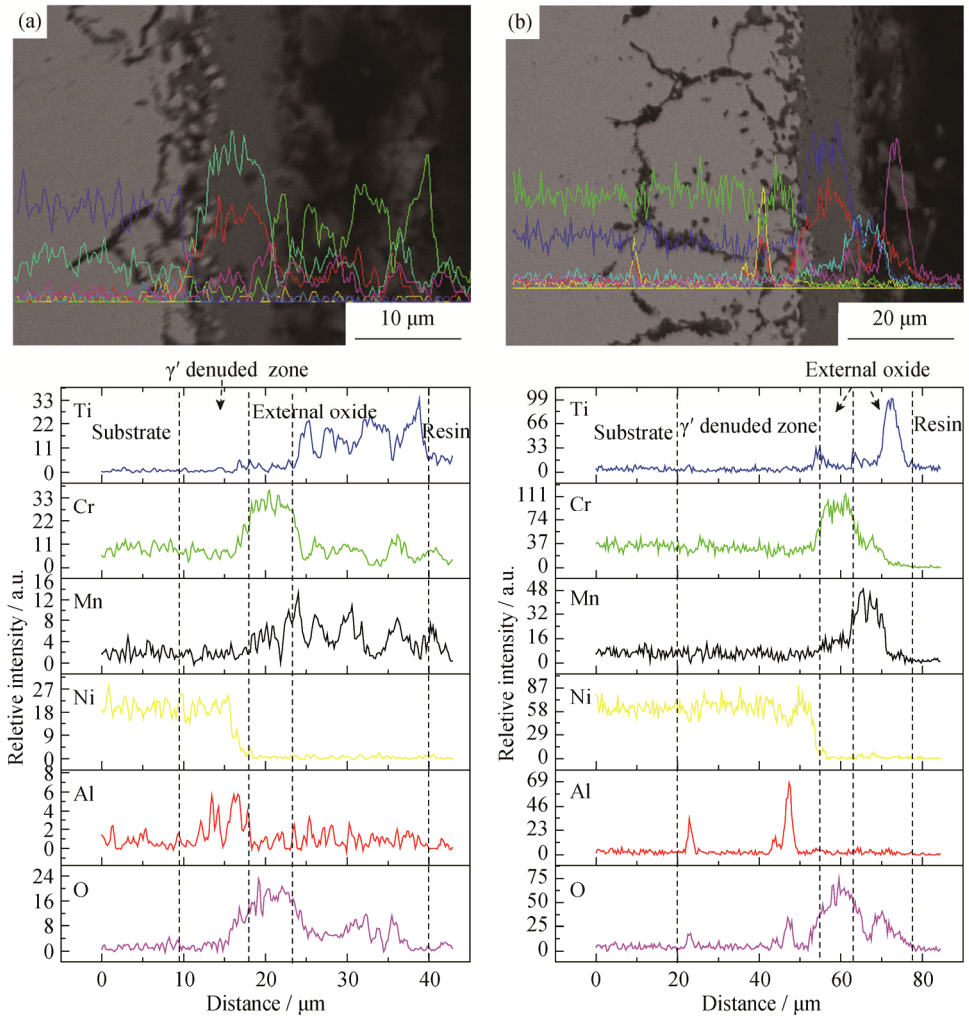

Fig. 9. EDS line scanning (and BSE images) of specimens oxidized isothermally at 1000°C for (a) 16 h and (b) 80 h, showing the distribution of elements along the cross-section.

4. Conclusions

(1) The weight-gain curve follows the parabolic law and constant k_p is 4.0623 × 10^{-5} $mg^2 \cdot cm^{-4} \cdot s^{-1}$ when the alloy is treated at 1000°C under experimental still air. The curve reveals that a continuous outer oxide layer was formed and that the weight-gain rate was controlled by the diffusion of O ions and the alloying elements.

(2) The external oxides formed on the alloy surface were confirmed as Cr_2O_3, TiO_2, and $MnCr_2O_4$. The relative contents of TiO_2 and $MnCr_2O_4$ increased under prolonged exposure. The columnar TiO_2 and underlying $MnCr_2O_4$ particles disrupted the continuity of the outermost oxide layer and accelerated the inward diffusion of O ions. The internal oxidation region increased from about 8 to about 35 μm after another 64 h of exposure. The internal oxides were composed of Al_2O_3 and TiN. The dendritic oxide Al_2O_3 distributed along the grain boundary, and a small amount of

TiN was formed on the tip of the Al_2O_3.

(3) The present nickel-based superalloy exhibited poor oxidation resistance at 1000°C. A series of oxides were also formed on the surface and sub-surface of the alloy. Fine TiO_2 particles dissolved with time in favor of the growth of more massive particles; the relationship was consistent with the mass gain curve.

Acknowledgements

The authors gratefully appreciate the financial support of Science and Technology Program of Jiangsu Province (Nos. BE2015144 and BE2015145) and the partner company, Jiangsu Shenyuan Special Steel Company.

References

[1] H. Naffakh-Moosavy, Microstructural evolution and castability prediction in newly designed modern third-generation nickel-based superalloys, *Int. J. Miner. Metall. Mater.*, 23(2016), No. 5, p. 548.

[2] J.H. Chen, P.M. Rogers, and J.A. Little, Oxidation behavior of several chromia-forming commercial nickel-base superalloys, *Oxid. Met.*, 47(1997), No. 5, p.381.

[3] S. Huang, L. Wang, X.T Lian, G.P. Zhao, F.F. Li, and X.M. Zhang, Hot deformation map and its application of GH4706 alloy, *Int. J. Miner. Metall. Mater.*, 21(2014), No. 5, p. 462.

[4] X.F. Liang, Y.T. Zhao, Z.H. Jia, and C. Zhang, Preparation and tensile properties of DD5 single crystal castings, *Int. J. Miner. Metall. Mater.*, 23(2016), No. 6, p. 683.

[5] S. Cruchley, H.E. Evans, M.P. Taylor, M.C. Hardy, and S. Stekovic, Chromia layer growth on a Ni-based superalloy: Sub-parabolic kinetics and the role of titanium, *Corros. Sci.*, 75(2013), No. 7, p. 58.

[6] Y.L. Xu, C.X. Yang, Q.X. Ran, P.F. Hu, X.S. Xiao, X.L. Cao, and G.Q. Jia, Microstructure evolution and stress-rupture properties of Nimonic 80A after various heat treatments, *Mater. Des.*, 47(2013), No. 9, p. 218.

[7] I.M. Edmonds, H.E. Evans, and C.N. Jones, The role of the γ′ precipitate dispersion in forming a protective scale on Ni-based superalloys at 750°C, *Oxid. Met.*, 73(2010), No. 1, p. 193.

[8] D. Kim, C. Jang, and W.S. Ryu, Oxidation characteristics and oxide layer evolution of alloy 617 and Haynes 230 at 900°C and 1100°C, *Oxid. Met.*, 71(2009), No. 5-6, p. 271.

[9] H. Singh, D. Puri, S. Prakash, and R. Maiti, Characterization of oxide scales to evaluate high temperature oxidation behavior of Ni–20Cr coated superalloys, *Mater. Sci. Eng. A*, 464(2007), No. 1-2, p. 110.

[10] S.Q. Zhao, X.S. Xie, and G.D. Smith, The oxidation behavior of the new nickel-based superalloy Inconel 740 with and without Na_2SO_4 deposit, *Surf. Coat. Technol.*, 185(2004), No. 2-3, p. 178.

[11] A. Jalowicka, W. Nowak, D.J. Young, V. Nischwitz, D. Naumenko, and W.J. Quadakkers, Boron depletion in a nickel base superalloy induced by high temperature oxidation, *Oxid. Met.*, 83(2015), No. 3, p. 393.

[12] F. Abe, H. Araki, H. Yoshida, and M. Okada, The role of aluminum and titanium on the oxidation process of a nickel-base superalloy in steam at 800°C, *Oxid. Met.*, 27(1987), No. 1, p. 21.

[13] W.F. Gale and T.C. Totemeier, *Smithells Metals* Reference *Book*, Elsevier Butterworth- Heinemann, Burlington, 2003, p. 13.

[14] C. Wagner, Oxidation of alloys involving noble metals, *J. Electrochem. Soc.*, 103(1956), No. 10, p. 571.

[15] J. Issartel, S. Martoia, F. Charlot, V. Parry, G. Parry, R. Estevez, and Y. Wouters, High temperature behavior of the metal/oxide interface of ferritic stainless steels, *Corros. Sci.*, 59(2012), p. 148.

[16] A.N. Blacklocks, A. Atkinson, R.J. Packer, S.L.P. Savin, and A.V. Chadwick, An XAS study of the defect structure of Ti-doped α-Cr_2O_3, *Solid State Ionics*, 177(2006), No. 33-34, p. 2939.

[17] A. Atkinson, M.R. Levy, S. Roche, and R.A. Rudkin, Defect properties of Ti-doped Cr_2O_3, *Solid State* Ionics, 177(2006), No. 19-25, p.1767.

[18] A. Naoumidis, H.A. Schulze, W. Jungen, and P. Lersch, Phase studies in the chromium-manganese-titanium oxide system at different oxygen partial pressures, *J.* Eur. *Ceram. Soc.*, 7(1991), No. 1, p. 55.

[19] D.R. Sigler, The oxidation behavior of Fe–20Cr alloy foils in a synthetic exhaust-gas atmosphere, *Oxid. Met.*, 46(1996), No. 5, p. 335.

[20] S.H. Song, Z.X. Yuan, and P. Xiao, Electrical properties of $MnCr_2O_4$ spinel, *J. Mater. Sci. Lett.*, 22(2003), No. 10, p. 755.

[21] G.R. Holcomb and D.E. Alman, The effect of manganese additions on the reactive evaporation of chromium in Ni–Cr alloys, *Scripta Mater.*, 54(2006), No. 10, p. 1821.